

On the terrestrial measurement of frame-dragging

Matthew P. Cartmell

Department of Mechanical & Aerospace Engineering, University of Strathclyde, Glasgow, G1 1XJ, Scotland, UK.

ABSTRACT

This paper considers the Foucault pendulum and its possible application as a measurement instrument for the relativistic effect of Lense-Thirring precession from frame-dragging. We discuss the Foucault pendulum under different forms of excitation. The first is through parametric excitation of the length, effective for overcoming natural aerodynamic and frictional dissipations and for amplification and ellipticity control of the response. The second is through coupling between a strong bob magnet and an exciter coil directly underneath, without the bob moving vertically at the frequency of parametric excitation. The achievements of the GP-B and LAGEOS missions in measuring frame-dragging in low Earth orbit are noted for comparison. The natural location for a frame-dragging measurement is polar and we derive an expression for Lense-Thirring precession using a gravitoelectromagnetic analogy for non-polar locations. The paper attempts to clarify the main challenges of this measurement.

1. Introduction

We start with the premise that an *inertial* frame is defined as one that is not accelerating in the usual detectable sense. General Relativity states that inertial frames are ‘influenced and dragged by the distribution and flow of mass–energy in the universe’, noting the relativistic equivalence of mass and energy [1]. This dragging of inertial frames is simply called frame-dragging and influences, for example, the flow of time around a spinning body.

A theory for frame-dragging was proposed by Lense and Thirring in 1918, in which inertial frames are dragged around a central *rotating* mass due to the effect of its angular momentum on the surrounding spacetime [2]. The rotation of the central mass twists the surrounding spacetime, which will perturb any nearby spinning gyroscope. For such a gyroscope in orbit around the Earth, for example, its axis of rotation will precess: this effect is known as Lense-Thirring precession, and henceforth as LT precession. In fact, Earth’s curvature of spacetime is capable of generating frame-dragging that is generally considered to be demonstrable in three gravitomagnetic manifestations:

- by the precession of a gyroscope in orbit around the Earth, just mentioned,
- by the precession of orbital planes, where a mass orbiting the Earth constitutes a gyroscope whose orbital axis will precess, under appropriate conditions, and
- by the precession of the periaapsis of the orbit of a test mass about the Earth.

GP-B measured the first two [3], and the LAGEOS satellites measured the second one only [4]. LAGEOS measured the LT drag of the satellite orbital planes to be ~ 0.031 arcsecs/year [1], which is $\sim 8.611 \cdot 10^{-6}$ °/year. This was subject to error

that was difficult to quantify, due to uncertainty in the Earth's mass distribution, and the effects of atmospheric drag, and there is still some debate about the true size of the error in LAGEOS's measurement, but it is thought mainly to have derived from the low eccentricity of the LAGEOS orbits and the difficulties in eliminating Earth multipoles. In contrast, GP-B measured LT to be ~ 0.037 arcsecs/year [1], which equates to $10.833 \cdot 10^{-6}$ °/year. GP-B used *IM Pegasi HR 8703* as the guide star and operated on a highly circular polar orbit of 642 km altitude [1]. The spin axes of GP-B's gyroscopes drifted and the geodetic precession [5] (due simply to the presence of the mass of Earth rather than its presence *and* its rotation) was itself measured to an impressive precision of 1.5 %. The total relativistic precession of such a spinning body is the vector sum of the LT and geodetic precessions, whose components in the case of GP-B were usefully at right angles to each other. Our main interest is the LT component. It is important to note that the relativistic frame-dragging effect evidenced by LT precession is about ten million times smaller than, for example, the classical Newtonian effects operating on the plane of the LAGEOS orbits, requiring an 'enormously accurate treatment of background effects' [6]. The analysis behind LT precession, in terms of (weak) gravitomagnetic effects on an accelerating mass, can be considered analogously with a circulating charge producing a magnetic field. Specifically, the analogy is between the equations that govern the torques on a spinning electric charge with magnetic moment μ moving through a magnetic field, and the torques on a spinning test-mass moving under the influence of a large and nearby rotating mass [1], and this analogy is made through Maxwell's equations which we return to later. Karl Schwarzschild [7] proposed an exact solution, now known as the Schwarzschild metric, for the tensor governing the space surrounding a large non-rotating spherical body, and this fully describes curved (non-Euclidean) space. On the other hand, the Kerr metric accounts for the rotation of the massive body [7], and the mean GP-B measurement of LT precession was within ~ 5 % of the value predicted by using the Kerr metric — but with a measurement error estimated at approximately ± 19 %. The general Kerr solution for LT precession is somewhat complicated, but in the vicinity of the Earth we are dealing with weak fields and non-relativistic velocities, so that the full form of general relativity is not necessary and a linearised version of the theory is sufficient [8]. If we consider spacetime to be stationary around the Earth, i.e. mass and fluid velocity distributions are unchanging, in spite of the Earth's rotation, then this simplifying stationarity can be used as a basis for a '3+1 slicing' of spacetime, in terms of the spatial (3) and time (1) dimensions. This means that the spacetime metric tensor $g_{\mu\nu}$ then decomposes naturally into constituent parts, and because of the prevailing conditions of weak gravity and non-relativistic (low) velocities this decomposition can be used to form the basis of a useful analogy with electromagnetism as expressed by Maxwell's equations, from which an expression for LT precession can eventually be obtained [8,9].

1.1 Lense-Thirring precession about the Earth

We start with gravitational analogies for the electromagnetic scalar and vector potentials taken from the Kerr spacetime metric, stated in terms of the time-time and time-space components, where c is the speed of light,

$$\Phi = \frac{1}{2}(g_{00} - 1)c^2$$

$$A_i = g_{0i}c^2. \tag{1}(2)$$

To get the analogies we take Maxwell's equations in their usual form,

$$\begin{aligned} \nabla \cdot \bar{E} &= \frac{\rho}{\epsilon_0} \\ \nabla \cdot \bar{B} &= 0 \\ \nabla \times \bar{E} &= -\frac{\partial \bar{B}}{\partial t} \\ \nabla \times \bar{B} &= \mu_0 \bar{J} + \mu_0 \epsilon_0 \frac{\partial \bar{E}}{\partial t}. \end{aligned} \tag{3)-(6)}$$

We then look at the physical context for Maxwell's equations. Equation (3) states that the quantity of electric field coming from a region of space is proportional to the total electric charge in that region of space. Equation (4) states that the magnetic field doesn't come or go but travels in a continuous loop. Equation (5) says that the curl of the electric field is equal to the negative of the rate of change of the magnetic field. Changing the magnetic field alters the curl of the electric field, with the negative sign defining that they go in opposite directions. So, the curl of the electric field pushes electric charge round in a circle in the form of an electric current. Finally, equation (6) says that the curl of the magnetic field is proportional to the current density and a changing electric field. Defining terms precisely: \bar{E} is the electric field, ρ is the electric charge density, ϵ_0 is the permittivity of free space, \bar{B} is the magnetic field, μ_0 is the permeability of free space, and \bar{J} is the current density. We then bring in the gravitoelectric field \bar{E}_G and the gravitomagnetic field \bar{H} and it is well known that they are related to the potentials of equations (1) and (2) according to the simplifying Lorentz gauge [10], as follows,

$$\begin{aligned} \bar{E}_G &= -\nabla\Phi - \frac{1}{4c} \frac{\partial \bar{A}}{\partial t} \\ \bar{H} &= \nabla \times \bar{A}. \end{aligned} \tag{7}(8)$$

In the analogy given by [8], the electric field of Maxwell's equations \bar{E} becomes the gravitoelectric field \bar{E}_G and the magnetic field of Maxwell's equations \bar{B} becomes the gravitomagnetic field \bar{H} . The electric charge density ρ becomes the mass density ρ_m . The charge current density \bar{J} becomes the mass current density defined by $G\rho_m\bar{v}$, where G is Newton's gravitational constant and \bar{v} is the velocity of the source mass. These substitutions are applied by means of the analogy in order to generate the gravitational analogue of Maxwell's electromagnetic equations,

$$\nabla \cdot \bar{E}_G = -4\pi G \rho_m$$

$$\nabla \cdot \bar{H} = 0$$

$$\nabla \times \bar{E}_G = 0$$

$$\nabla \times \bar{H} = 4 \left[-4\pi G \frac{\rho_m \bar{v}}{c} + \frac{1}{c} \frac{\partial \bar{E}_G}{\partial t} \right].$$

(9)-(12)

Despite some structural similarities between the equations which emerge from the gravitational analogy, (9)-(12), and Maxwell's equations themselves, equations (3)-(6), there are still some qualifiers and provisos to be made, [8] as follows:

- gravity is attractive, but electromagnetism is both attractive and repulsive (this difference leads to the minus signs in the RHS 'source terms' in equations (9) and (12),
- the gravitational tensor introduces the additional 4 in equation (12),
- the space-space components from the gravitational metric tensor correspond to curved space rather than Euclidean space. As we are only interested here in the effects of the Earth's rotation on an orbiting test mass then we can neglect the curvature of space and also those terms that are not gravitometric and of the order of $\left(\frac{v}{c}\right)^2$.

Assuming that equations (9)-(12) can be used to find the gravitoelectric and gravitomagnetic fields, the force on an orbiting test mass can be found from,

$$\bar{F} = m\bar{E}_G + \frac{m}{c} \bar{v} \times \bar{H}$$

(13)

from which we get,

$$m \frac{d\bar{v}}{dt} = -\frac{\alpha}{r^2} \bar{n} + \frac{m}{c} \bar{v} \times \bar{H}$$

(14)

and where $\bar{r} = r\bar{n}$ is the orbital radius vector of the test mass m and $\alpha = GMm$, where M is the mass of the Earth. We recall that \bar{H} is the gravitomagnetic field due to the Earth's rotation and note that this can be found from equations (9)-(12). Because, in general, the magnetic moment is given by,

$$\bar{\mu} = \frac{1}{2c} \int [\bar{r} \times \bar{j}] dV$$

where \bar{j} is the electric current density, so the gravitational analogy leads to,

$$\bar{\mu}_G = -4G \frac{1}{2c} \int \rho_m [\bar{r} \times \bar{j}] dV = -2G \frac{\bar{S}}{c}$$

(15)

where $\bar{S} = \int \rho_m [\bar{r} \times \bar{j}] dV$, this being the rotating gravitating body's proper angular momentum. The conventional magnetic moment $\bar{\mu}$ creates a dipole magnetic field, given by,

$$\bar{B} = \frac{3\bar{n}(\bar{n} \cdot \bar{\mu}) - \bar{\mu}}{r^3}$$

so, inserting $\bar{\mu}_G$ instead of μ leads to a form which now represents the Earth's dipolar gravitomagnetic field,

$$\bar{H} = \frac{2G}{c} \left[\frac{\bar{S} - 3\bar{n}(\bar{n} \cdot \bar{S})}{r^3} \right]. \quad (16)$$

The abstract angular momentum for the large rotating body \bar{S} can be replaced by the angular momentum specific to the Earth, defined as \bar{L} in [8], so we can extract the Earth's angular velocity as,

$$\bar{\Omega} = \frac{2G}{c^2 r^3} \bar{L}. \quad (17)$$

Therefore, the gravitomagnetic field stated in equation (16) can now be restated in terms of the Earth's angular velocity, where $\bar{S} \equiv \bar{L}$, noting that it is divided by the velocity of light in order to accommodate equation (17) correctly,

$$\frac{\bar{H}}{c} = \bar{\Omega} - 3\bar{n}(\bar{\Omega} \cdot \bar{n}). \quad (18)$$

In order to proceed to the LT precession we need to revert to explicit angular momentum of the Earth, through equation (17) and then rearrange to get the gravitomagnetic field in terms of fundamental quantities and in the conventional form, as follows,

$$\bar{H} = \frac{4G}{c} \left[\frac{\bar{L}r^2 - 3\bar{r}(\bar{L} \cdot \bar{r})}{2r^5} \right]. \quad (19)$$

One can find the same result for \bar{H} in [10] although the notation and the aggregation of constants is done differently there. Before we complete the analysis for the LT precessional term we state the general expression for the spin precession rate for LT from the Schiff formula statement of the LT metric [11], which is,

$$\bar{\Omega}_{Tot} = \bar{\Omega}_{Th} + \bar{\Omega}_{Geo} + \bar{\Omega}_{LT} \quad (20)$$

where $\bar{\Omega}_{Tot}$ is the total angular velocity measured, assuming an orbital test mass such as a satellite containing gyroscopic measurement instruments. The right-hand side terms of equation (20) are the Thomas precession $\bar{\Omega}_{Th}$, the geodetic precession $\bar{\Omega}_{Geo}$, and the LT precession $\bar{\Omega}_{LT}$. Concentrating on the LT precession, averaging over fast

orbital motions [8] and persevering with the notation of [8], we find [12] that LT is directly equal to,

$$\bar{\Omega}_{LT} = \frac{\bar{H}}{2c} \quad (21)$$

and so for a closely orbiting body equation (19) gives this for the averaged gravitomagnetic field at the poles,

$$\bar{H}_{poles} = \frac{4G \bar{L}'}{c r^3} \quad (22)$$

and if we now move from a general closely orbiting body to a specific terrestrial location where there is a body elevated at h from the surface of the Earth (therefore at altitude R , where $R = r_E + h$, and r_E is the radius of the Earth at the location), then the LT precession from equation (19) is given for both northern and southern latitudes, by,

$$\Omega_{LT} = \frac{G}{c^2 R^3} L' |1 - 3|\bar{z} \cdot \bar{r}||. \quad (23)$$

The scalar angular momentum L' is given by $L' = I_{\oplus} \Omega_{\oplus}$, and considering the Earth initially as a non-oblate sphere then $I_{\oplus} = \frac{2}{5} M r_E^2$. But the actual radius of gyration of the Earth is $0.576 r_E$ [13], so the factor of $\frac{2}{5}$ becomes 0.576^2 which is 0.3316. Therefore $I_{\oplus} = 0.3316 M r_E^2$, from which we obtain,

$$\Omega_{LT} = \frac{0.3316 GM \Omega_{\oplus}}{c^2 R} |1 - 3|\cos\theta|| \quad (24)$$

where $\bar{z} \cdot \bar{r} = \cos\theta$ and $R \approx r_E$ for h very small indeed. This result does not include the geodetic precession and is purely the LT component. The angle θ is the colatitude which is the included angle between \bar{z} and \bar{r} (the spin axis of Earth and the local vertical axis at the location, respectively) so $\theta = \frac{\pi}{2} - \phi$, where ϕ is the latitude as measured north or south from the equator. At the poles, from equation (22), we get a reduced form of equation (23) as follows,

$$\Omega_{LT} = \frac{2G}{c^2 R^3} L' (\bar{z} \cdot \bar{z}). \quad (25)$$

This simplifies to the following after making the appropriate substitutions,

$$\Omega_{LT} = \frac{0.6632 GM \Omega_{\oplus}}{c^2 R} \cos\theta. \quad (26)$$

1.2 Theoretical predictions for LT precession at the North Pole and at Glasgow

The following numerical data can be used to calculate the precession both at the North Pole and at Glasgow: $G = 6.67408 \cdot 10^{-11} \text{ m}^3 \text{ kg}^{-1} \text{ s}^{-2}$, $M = 5.972 \cdot 10^{24} \text{ kg}$, $\Omega_{\oplus} = 7.2921150 \cdot 10^{-5} \text{ rad/s}$, $c = 2.99792488 \cdot 10^8 \text{ m/s}$, $R = 6356 \cdot 10^3 \text{ m}$ at the North Pole, $R = 6363.18 \cdot 10^3 \text{ m}$ at Glasgow, $\phi = 1.5707963 \text{ rad}$ at the North Pole, $\phi = 0.9750 \text{ rad}$ at Glasgow. Pippard [14] gives the LT precession as 220 mas/year at the North Pole. Ruggiero & Tartaglia [12] state the LT precession at the North Pole to be 281 mas/year. Using equations (24) or (26) and the above data we get $\Omega_{LT} = 219.5 \text{ mas/year}$ at the North Pole. By changing both the latitude and the radius of the Earth to the values for the location of Glasgow the LT precession there can be calculated using equation (24) to be $\Omega_{LT} = 162.6 \text{ mas/year}$.

2. Calculation of LT precession at co-latitude θ

The LT precession measured at co-latitude θ is given by equation (27) and comprises the measured precession of the pendulum bob m with respect to the Earth (first RHS term) minus the apparent precession associated with a guide star relative to the Earth (second RHS term) minus the precession of the pendulum relative to the guide star (third/fourth RHS term), as first explained in [15]. At the poles the third/fourth terms go to zero because θ is zero at both poles. The immediate objective is to calculate a typical numerical value for the third/fourth terms for Glasgow to see how they will influence $\Omega_{LT\theta}$.

$$\Omega_{LT\theta} = \Omega_{FP_{m/E}} - \Omega_{gs/E} - \Omega_{\oplus}(1 - \cos \theta) \quad (27)$$

The WGS-84 local terrestrial gravity model [16] can be inverted to get ϕ from g_{local} ,

$$g_{local} = g_{eq} \left(\frac{1 + k \sin^2 \phi}{\sqrt{1 - \varepsilon^2 \sin^2 \phi}} \right)$$

where,

$$\varepsilon^2 = 1 - \left(\frac{b}{a} \right)^2$$

$$k = \frac{(b g_p - a g_{eq})}{a g_{eq}}$$

$$\theta = \frac{\pi}{2} - \phi.$$

(28-31)

The acceleration due to gravity measured at the experimental site, g_{local} , could be detected from a MEMS gravimeter as a continuous signal over time, and if we take g_{eq} , g_p , a , b as known values that can be input to a calculation based around the WGS-84 local terrestrial gravity model [16,17,18] (given in equations (28)-(30)) then we can obtain a corresponding value for latitude, ϕ . From that we can easily

calculate the associated co-latitude, θ , using equation (31). The gravimeter will give a fluctuating value for g_{local} over time, and this will have an upper and lower value, and a nominal value, with corresponding values for ϕ , which we define as, ϕ_U, ϕ_L , and ϕ_N , respectively. See Figure 1 for details of a typical time response for the prototype MEMS device of [19]. This means we can calculate three values for the co-latitude too, using equation (31), giving θ_U, θ_L , and θ_N . From that we can calculate the value of the right-hand-side third and fourth terms, as follows,

$$\Omega_{T_{3\&4}} = -\Omega_{\oplus}(1 - \cos \theta) \quad (32)$$

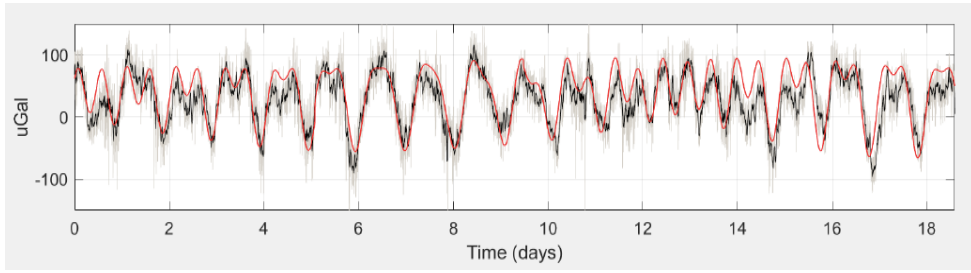


Figure 2.1 Measurement of fluctuations in the local gravitational acceleration in the city of Glasgow, Scotland, reproduced with the permission of the authors of [19].

If we take the upper, lower, and nominal values of the third/fourth terms of the right-hand-side of equation (27) we get this, $\Omega_{T_{3\&4U}} = -\Omega_{\oplus}(1 - \cos \theta_U)$, $\Omega_{T_{3\&4L}} = -\Omega_{\oplus}(1 - \cos \theta_L)$ and $\Omega_{T_{3\&4N}} = -\Omega_{\oplus}(1 - \cos \theta_N)$

(33)-(35)

The three values of g_{local} can be found to be as follows from published data for Glasgow, Scotland [17], noting the predicted fluctuation of around $\pm 100 \mu\text{Gal}$ of Figure 2.1 which equates to $\pm 0.000001 \text{ m/s}^2$: $g_{localU} = 9.8156 + 0.000001 = 9.815601 \text{ m/s}^2$, $g_{localL} = 9.8156 - 0.000001 = 9.815599 \text{ m/s}^2$, $g_{localN} = 9.8156 \text{ m/s}^2$. Using the WGS-84 model [16] with free air correction for elevation of Glasgow at $h = 38 \text{ m}$, we get the following latitude fluctuations: $\phi_U = 0.973206 \text{ rad/s}$, $\phi_L = 0.973165 \text{ rad/s}$, and $\phi_N = 0.973186 \text{ rad/s}$. Therefore, equation (31) gives, $\theta_U = 0.597589 \text{ rad/s}$, $\theta_L = 0.597631 \text{ rad/s}$, and $\theta_N = 0.597610 \text{ rad/s}$.

Substituting the values for θ_U, θ_L , and θ_N into equations (33)-(35), taking $\Omega_{\oplus} = 7.2921150 \times 10^{-5} \text{ rad/s}$, gives the following upper, lower, and nominal predicted values for the third and fourth terms of the right-hand-side of equation (27) and the right-hand-side of equation (32), $\Omega_{T_{3\&4U}} = -0.0000126376 \text{ rad/s}$, $\Omega_{T_{3\&4L}} = -0.0000126393 \text{ rad/s}$, and $\Omega_{T_{3\&4N}} = -0.0000126385 \text{ rad/s}$. Converting these values from rad/s to mas/year requires a multiplicative conversion factor of 6.50477×10^{15} leading to: $\Omega_{T_{3\&4U}} = -8.2204934323 \times 10^{10} \text{ mas/year}$, $\Omega_{T_{3\&4L}} = -8.2216143848 \times 10^{10} \text{ mas/year}$, and $\Omega_{T_{3\&4N}} = -8.2210538999 \times 10^{10} \text{ mas/year}$. The numerical range of the third and fourth right-hand-side terms shows how significant their contribution is to the measurement of LT precession, and is

given by $\Omega_{T_{3\&4U}} - \Omega_{T_{3\&4L}}$, for which we get an absolute value of, $|\Omega_{T_{3\&4U}} - \Omega_{T_{3\&4L}}| = 1.12095 * 10^7$ mas/year. As we have seen, this range is due to a fluctuation in $g_{local} = \pm 100 \mu\text{Gal}$ and so it is confirmed that these terms will dominate the measurement defined by equation (27). Results have also been obtained for $g_{local} = \pm 0 \mu\text{Gal}$, $g_{local} = \pm 50 \mu\text{Gal}$, $g_{local} = \pm 75 \mu\text{Gal}$, $g_{local} = \pm 125 \mu\text{Gal}$, and $g_{local} = \pm 150 \mu\text{Gal}$, and the values calculated for $Range_{T_{34}} = |\Omega_{T_{3\&4U}} - \Omega_{T_{3\&4L}}|$, and plotted on the graph shown in Figure 2.2.

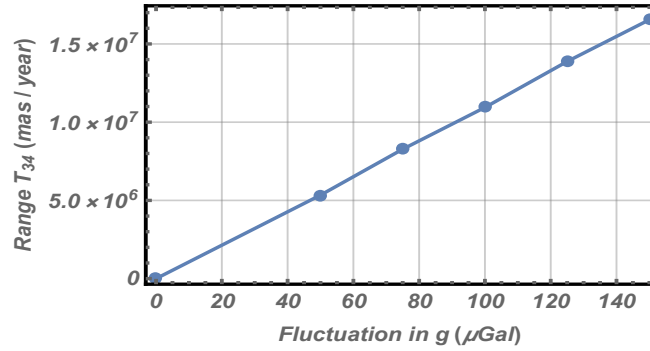


Figure 2.2 $Range_{T_{34}}$ as a function of \pm fluctuations in the local gravitational acceleration in the city of Glasgow, Scotland.

The linear relationship in Figure 2.2 confirms that the lower the measured fluctuation in g_{local} the lower the value of the range of terms T_{34} in equation (27), and therefore the correspondingly reduced dominance of these terms within $\Omega_{LT\theta}$. Note that a measurement of Earth motion is required to define numerically the second term on the right-hand side of equation (27). This will be obtained via online data from [20], however a detailed discussion of this is outside the scope of this present paper and is reserved for a future publication.

3. Pendulum tracking geometry

The motion of the pendulum has to be measured in such a way that the extremely small component due to LT precession is detectable. The primary requirement is for a non-contacting measurement system that can track the pendulum's motion continuously over time, and resolve the LT component. High resolution cameras and autocollimators were considered but it was clear that in the case of the former the necessary resolution would only be available at extremely high cost, and the autocollimator option comes with a considerable additional complication in terms of the necessary tracking instrumentation and control. It was decided to pursue a different approach in which an optical beam-crossing system using a small array of four laser line generators can be used to detect the presence of the pendulum bob. Sequential information extracted from this system can then be used then to infer the instantaneous position of the bob periodically, and then the time-base associated with the continuous sampling of that data can be used to detect the small shifts in the timing of key points in the sequence, to detect and quantify the LT precession. We now summarise the three beam crossing geometries, in sub-sections 3.1 to 3.3.

3.1 Pendulum swing plane orthogonal to the optical transmission path

This measurement geometry analysis initially assumes that the swing plane of the precessing pendulum is instantaneously orthogonal to the optical path of the array of four laser line generators. This is one of three cases for which a precise analysis is needed to be able to compute the overall time taken to cross the optical transmission path. We consider two half-periods, where the pendulum initially swings from left to right and then from right to left, to cover one complete swing that is perfectly orthogonal to the optical transmission path. The four beams are denoted Top Left (TL), Bottom Left (BL), Top Right (TR), and Bottom Right (BR), and each of the four transmitters is located exactly opposite a specific receiver. When the bob interrupts a beam the associated receiver's output goes to a logical low. An uninterrupted beam generates a logical high at its corresponding receiver output.

3.1.1 Pendulum swinging left to right:

- (a) Bob sets TL & BL low as it grazes the beam on approach,
- (b) TL, BL, TR, BR – all low as bob is exactly central,
- (c) Bob sets TR & BR low as it grazes the beam on departure.

3.1.2 Pendulum swinging right to left:

- (a) Bob sets TR & BR low as it grazes the beam on approach,
- (b) TR, BR, TL, BL – all low as bob is exactly central,
- (c) Bob sets TL & BL low as it grazes the beam on departure.

3.1.3 Analysis of swing in either direction

The period of the pendulum is T and this is given by, $T = \frac{1}{f_n}$ sec. Therefore, one half period; either a left-to-right or right-to-left swing takes, $\frac{T}{2} = \frac{1}{2f_n}$ sec. This is the time it takes to swing through one peak-to-peak amplitude. The peak-to-peak amplitude is defined by $2a$ where a is the peak amplitude of swing. The bob diameter is d_B so the time in seconds that it takes the bob to swing through a distance equal to its own diameter is,

$$t_{d_B} = \frac{d_B}{4af_n}. \quad (36)$$

To calculate this time we need to know the bob diameter and the pendulum natural frequency of free undamped vibration, and also the peak amplitude. We have to fix d_B and f_n to build the pendulum, and we can estimate a , by assigning a range of values to it so that we can get a corresponding range of values for t_{d_B} . For this case the bob centre covers distance $2d_B$ from the instant the bob grazes the beam as it approaches, to the instant that it still (just) grazes the beam as it departs. So, the overall interrupt time from start to finish for this case is given by $2t_{d_B}$.

Hence we get,

$$t_{2d_B} = \frac{d_B}{2af_n} = \frac{\pi d_B}{a\sqrt{\frac{g}{l_0}}} \quad (37)$$

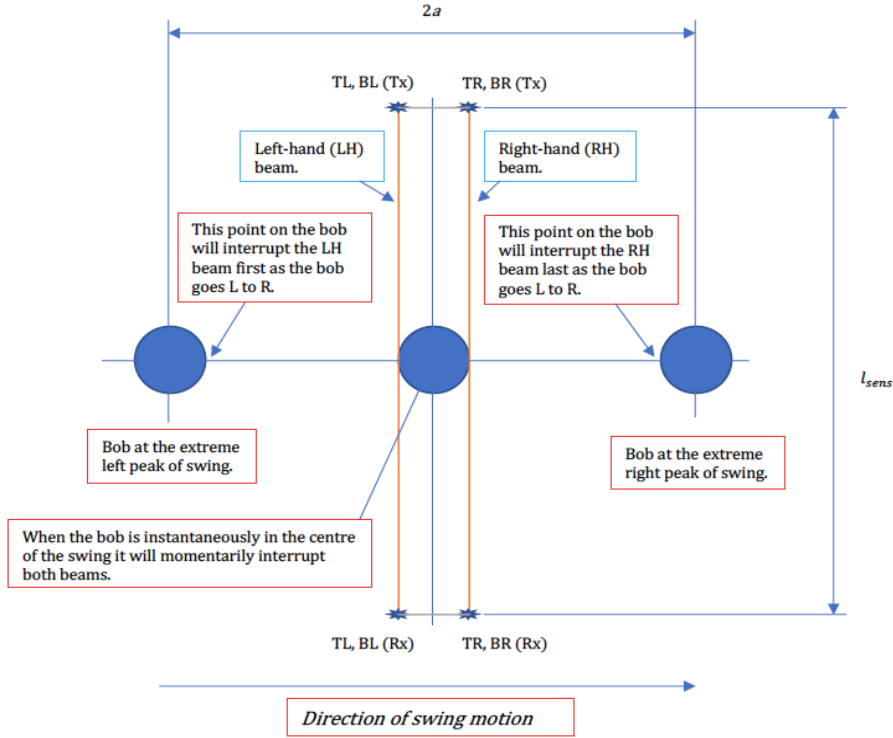


Figure 3.1 Beam crossing geometry: case 1, showing plan view of the bob travelling left to right, exactly the same principles apply in reverse when the bob is travelling right to left. Note also that $l_{sens} > 2a$ so that the pendulum can swing freely when moving under case 3 - see Figure 3.3 below. Key: TL = Top Left sensor, TR = Top Right sensor, BL = Bottom Left sensor, BR = Bottom Right sensor, Tx = laser transmitters, Rx = laser receivers.

where g is the local acceleration due to gravity and l_0 is the effective length of the pendulum. The actual time taken for the beam interrupts for the orthogonal geometry case depends on the precise geometry of the design. So, the beams are designed to be set up so that when the bob is exactly central in its swing it interrupts both beams. Very fine mechanical adjustment will be available to set this up exactly, using high precision parts that are guaranteed to be stable over the planned range of operating temperature. Therefore, the time is exactly governed by twice the diameter of the bob, and is defined by t_{2d_B} . This is because the centre of the bob is at $d_B/2$ to the left of the beam just when the RH side of the bob starts to graze the beam on the approach side, then there is the distance between the beams which is defined by d_B , and then the centre of the bob goes through $d_B/2$ again before the LH side of the

bob finally stops interrupting the beam on the departure side. This principle is the same whether it's swinging left-to-right or right-to-left.

3.2 Pendulum swing plane located at an arbitrary angle of precession

In this case the pendulum has precessed through Ω so that the swing plane is no longer orthogonal to the optical transmission path, and instead is at an arbitrary precessional angle of Ω . In that case the geometry is such that the bob has to cover a longer distance d_{pp} to pass across the optical transmission path, and that distance is given by the following where Ω is in degrees,

$$d_{pp} = 2d_B + (2a - 3d_B) \frac{\Omega}{90}. \quad (38)$$

This means that the time to cover the TL, BL pair and then the TR, BR pair is a little longer than for the case of 3.1, and is found as follows,

$$t_{d_{pp}} = \frac{d_{pp}}{4af_n} = \frac{\pi(2d_B + (2a - 3d_B) \frac{\Omega}{90})}{2a \sqrt{\frac{g}{l_0}}} \text{ sec. (where } t_{d_{pp}} < \frac{T}{2}, \text{ and } \frac{T}{2} = \frac{1}{2f_n} = \frac{\pi}{\sqrt{\frac{g}{l_0}}}). \quad (39)$$

This time reaches a maximum as Ω tends to 90° and at that point we move to the final geometrical case (given in 3.3 below). Conversely, when $\Omega = 0$ we get $t_{d_{pp}} = \frac{\pi d_B}{a \sqrt{\frac{g}{l_0}}}$ and this is the same as t_{2d_B} . So, this case then degenerates down to the first geometrical configuration of case 3.1. In general, assuming we approach from bottom left (looking down) we have this sequence,

- (a) Bob sets TL & BL low as it grazes beam on approach,
- (b) TL, BL, TR, BR – all low as bob is central,
- (c) Bob sets TR & BR low as it grazes beam on departure,
- (d) Bob sets TR & BR low as it grazes beam on approach,
- (e) TR, BR, TL, BL – all low as bob is central,
- (f) Bob sets TL & BL low as it grazes beam on departure.

3.3 Swinging exactly along the optical transmission path.

This simple case is shown in Figure 3.3 in which both the beams are continually interrupted for the whole of the time that the swing plane of the pendulum is aligned with the optical transmission path. This is the case when $\Omega = 90^\circ$. The time that the sensors are low over one half period is exactly equal to the half period itself. They will stay low for the remaining half period.

The three cases given above cover all possible motions of the precessing pendulum and provide the necessary theoretical basis for designing the measurement instrumentation discussed in section 6.

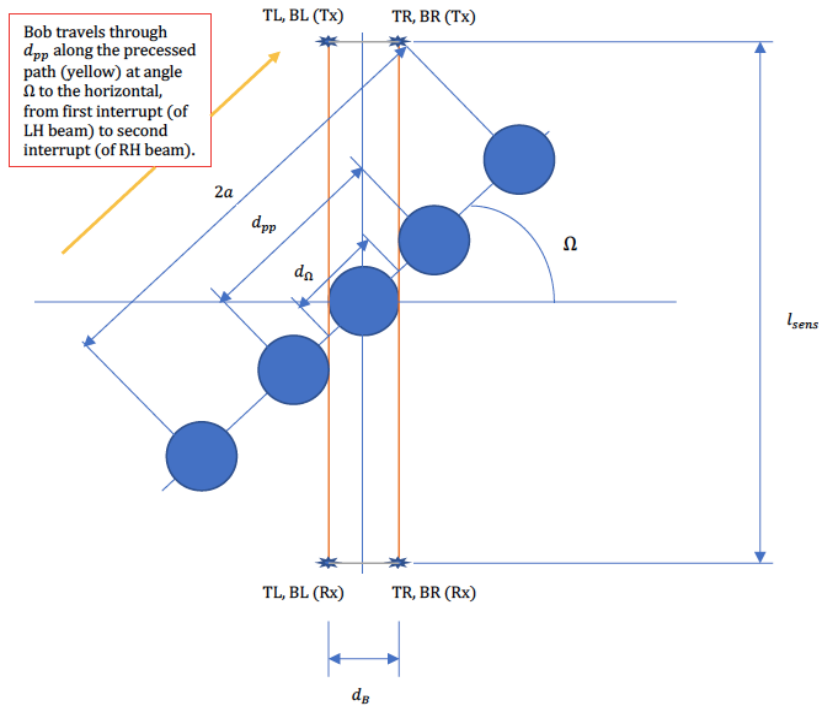


Figure 3.2 Beam crossing geometry: case 2, plan view of the bob going left to right along a path precessed at Ω to the horizontal, same principles apply for right to left (see (a)-(f) below). Key: TL = Top Left sensor, TR = Top Right sensor, BL = Bottom Left sensor, BR = Bottom Right sensor, Tx = laser transmitters, Rx = laser receivers.

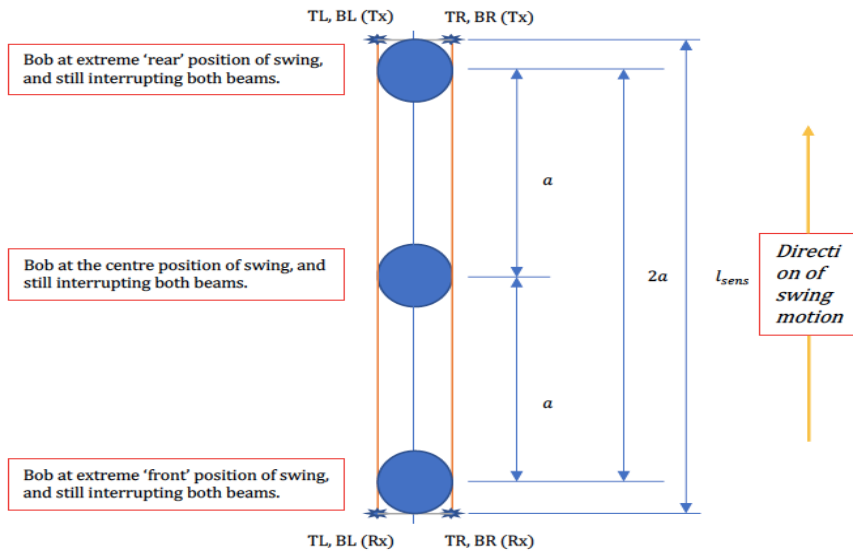


Figure 3.3 Beam crossing geometry: case 3, showing plan view of the bob travelling front to back along a path exactly aligned with the sensor light paths ($\Omega = 90^\circ$), noting that the same principles apply when travelling back to front. Key: TL = Top Left sensor, TR = Top Right sensor, BL = Bottom Left sensor, BR = Bottom Right sensor, Tx = laser transmitters, Rx = laser receivers.

4. Electromagnetic pendulum exciter system

4.1 Ellipticity control

We now summarise the original work of Schumacher and Tarbet [21]. It is repeated in full here, because it is central to the effective operation of the practical system.

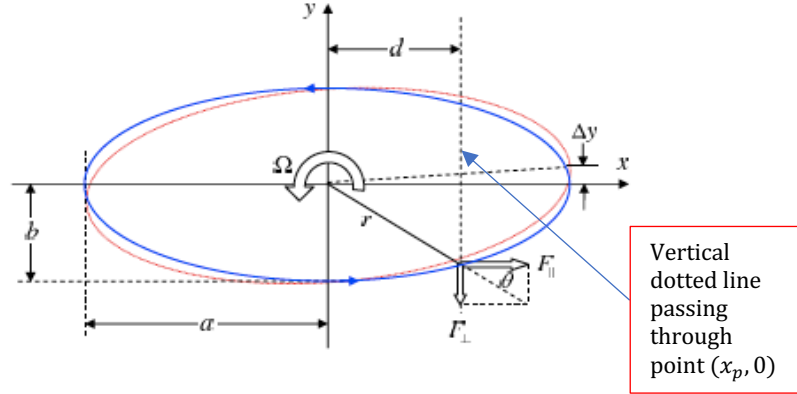


Figure 4.1 Reproduced from [21] with the permission of the authors. The original caption in [21] stated: Planar view of the approximate path of a spherical pendulum with semi-major axis a and semi-minor axis b that is moving in a counter-clockwise ellipse. The suspension is centred on the z -axis above the origin. The pendulum is precessing at rate Ω , and in one full cycle the apex advances by a distance Δy , as suggested by the light dotted and rotated ellipse. The impulsive driving force is applied at $x = d$, and it is resolved into components parallel and perpendicular to the major axis. The minor axis can be larger or smaller, resulting in a b -dependent magnitude of the transverse force F_{\perp} for a fixed longitudinal force F_{\parallel} .

The methodology for excitation and also ellipticity control first proposed in [21] uses two concentric electromagnetic sensing and pusher coils to maintain planar motion of the pendulum after launch. This approach has been chosen here over parametric excitation of the length [14, 23, and 24], because it offers a mechanically more robust and simple solution, with the added and very important advantage of offering ellipticity minimisation control that is independent of the magnitude of the minor axis of any residual ellipticity after the pendulum has first been launched. This, together with the fact that it does not in any way intrude on the natural motion of the Foucault pendulum, makes it by far the best approach for pendulum forcing. We start with reference to Figure 4.1, adopted from the original work of [21]. The excitation comes from an impulsive force applied electromagnetically to the bob, resolved into two components, F_{\perp} and F_{\parallel} . The parallel component, F_{\parallel} is the bigger of the two and overcomes the dissipation in the system, mainly due to aerodynamic damping and pivot friction. The transverse component, F_{\perp} is used to stop the intrinsic precession of the pendulum, and the objective of the analysis that follows is to relate this to distance d , which defines the point where the impulse excitation force has to occur to stop the unwanted intrinsic precession Ω . It is shown in [21] that d is independent of b . It is shown in detail in [21] that as the pendulum goes from $x = -a$ to $x = +a$ (effectively half a period) it takes $\frac{\Omega T}{2}$ seconds, and the associated precession angle is ϕ . The apex of the ellipse moves through distance Δy . The requirement is therefore for that distance Δy to be reduced to zero by means of an impulse applied at the time when the bob, travelling left to right, crosses the dotted line passing through the point

$(x_p, 0)$, after which it passes on through the distance $(a - d)$ to arrive at $(a, 0)$. The momentum associated with the force component F_{\perp} (which performs the neutralisation of the precession associated with Δy) is therefore given by,

$$m\Delta v_y = F_{\perp}\Delta t \quad (40)$$

where Δv_y is the velocity associated with the displacement Δy . The time Δt is the duration of the applied force and as $\Delta t \ll T$ it is appropriate to use the impulsive form of Newton's second law.

Now, the response of the pendulum in the x direction is simply expressed by $x(t) = a \sin \omega_0 t$ where the natural frequency of free undamped oscillation of the pendulum is defined by $\omega_0 = \sqrt{\frac{g}{l}}$ and we note that it takes a definable time t_d for the bob to travel from the origin to the dotted line shown in Figure 4.1 passing through the point $(x_p, 0)$. If $x(t) = d$ then $\frac{d}{a} = \sin \omega_0 t_d$, and this leads to $t_d = \frac{1}{\omega_0} \sin^{-1} \frac{d}{a}$. The geometry of the intrinsic precession shown in Figure 4.1 leads to,

$$\Delta y = \Delta v_y \left(\frac{T}{4} - t_d \right) = a \frac{\Omega T}{2} \quad (41)$$

and combining t_d and the first part of equation (41) gives,

$$\Delta y = \Delta v_y \left(\frac{T}{4} - t_d \right) = \Delta v_y \left(\frac{T}{4} - \frac{1}{\omega_0} \sin^{-1} \frac{d}{a} \right) = \frac{\Delta v_y}{\omega_0} \left(\frac{T\omega_0}{4} - \sin^{-1} \frac{d}{a} \right)$$

where $\frac{T\omega_0}{4} = \frac{\pi}{2}$ because $\omega_0 = 2\pi f_0$ and $f_0 = \frac{1}{T}$. So $\omega_0 = \frac{2\pi}{T}$ and $\frac{T\omega_0}{4} = \frac{\pi}{2}$.

From this, one gets $\Delta y = \frac{\Delta v_y}{\omega_0} \left(\frac{\pi}{2} - \sin^{-1} \frac{d}{a} \right)$.

Using the inverse trigonometrical identity $\cos^{-1} A = \frac{\pi}{2} - \sin^{-1} A$ the last equation simplifies down to,

$$\Delta y = \frac{\Delta v_y}{\omega_0} \cos^{-1} \frac{d}{a} \quad (42)$$

The force components F_{\perp} and F_{\parallel} are shown in Figure 4.1 at an arbitrary point on the ellipse, defined by coincidence with the dotted line passing through the point $(x_p, 0)$ and at angle θ to the x-axis. So, we have $\frac{F_{\perp}}{F_{\parallel}} = \tan \theta = \frac{y}{d}$. An ellipse is defined by $\left(\frac{x}{a}\right)^2 + \left(\frac{y}{b}\right)^2 = 1$ and from the equation above we have $F_{\perp} = F_{\parallel} \frac{y}{d}$, so the ellipse equation gives $y = b \sqrt{1 - \left(\frac{x}{a}\right)^2}$ and therefore we get the following for F_{\perp} ,

$$F_{\perp} = F_{\parallel} \frac{b}{d} \sqrt{1 - \left(\frac{d}{a}\right)^2} \quad (43)$$

This gives the transverse impulse force component F_{\perp} in terms of the longitudinal component F_{\parallel} , a , b , and d . Next, we take equations (40)-(43) inclusive, and Olsson's expression for Foucault pendulum intrinsic precession [22] which is given by,

$$\Omega = \frac{3}{8} \omega_0 \frac{ab}{l^2}. \quad (44)$$

Then first of all, Δy can be expressed by using equations (41) and (44),

$$\Delta y = \frac{1}{2} a \left(\frac{3}{8} \omega_0 \frac{ab}{l^2} \right) \left(\frac{2\pi}{\omega_0} \right) \quad (45)$$

Next equations (40), (42), and (43) are invoked, to get,

$$\Delta y = \frac{1}{m} \Delta t \frac{1}{\omega_0} F_{\parallel} \frac{b}{d} \sqrt{1 - \left(\frac{d}{a}\right)^2} \cos^{-1} \frac{d}{a} = \frac{F_{\parallel} \Delta t b}{m \omega_0 d} \sqrt{1 - \left(\frac{d}{a}\right)^2} \cos^{-1} \frac{d}{a} \quad (46)$$

Finally, if the right-hand sides of equations (45) and (46) are equated then it is possible to obtain,

$$\frac{1}{2} a \left(\frac{3}{8} \omega_0 \frac{ab}{l^2} \right) \left(\frac{2\pi}{\omega_0} \right) = \frac{F_{\parallel} \Delta t b}{m \omega_0 d} \sqrt{1 - \left(\frac{d}{a}\right)^2} \cos^{-1} \frac{d}{a}.$$

This reduces down to,

$$\frac{3 a^2 b \pi m \omega_0}{8 l^2 F_{\parallel} \Delta t} = \frac{b}{d} \sqrt{1 - \left(\frac{d}{a}\right)^2} \cos^{-1} \frac{d}{a}.$$

Then further to,

$$\frac{3}{4} Q \frac{ab}{l^2} = \frac{b}{d} \sqrt{1 - \left(\frac{d}{a}\right)^2} \cos^{-1} \frac{d}{a} \quad (47)$$

where,

$$Q = \frac{\pi m a \omega_0}{2 F_{\parallel} \Delta t}. \quad (48)$$

It can be seen that b cancels in equation (47), which is an important result in itself. The quantity represented by Q is formally defined as the quality factor ‘ Q ’, and in equation (48) this is the ratio of the momentum of the bob at the zero crossing and the momentum kick that it receives when the impulsive force is applied. Equation (47) is simplified further in [21] by introducing the nondimensionalised quantities $\alpha = \frac{a}{l}$ and $\delta = \frac{d}{a}$, to lead to this expression of nullification,

$$\frac{3}{4}Q\alpha^2 = \frac{1}{\delta}\sqrt{1-\delta^2}\cos^{-1}\delta.$$

(49)

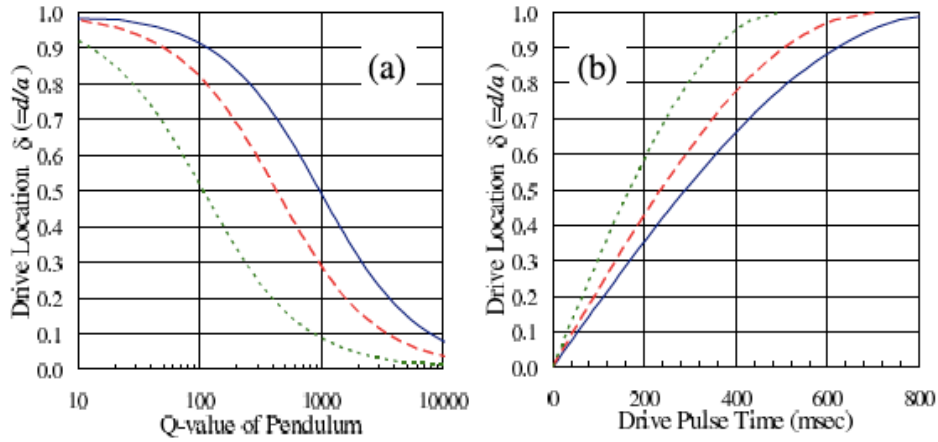


Figure 4.2 Reproduced from [21] with the permission of the authors. The original caption in [21] stated: (a) For three pendulum lengths (L) with amplitude of 0.15 meter, the relationship of the scaled driving distance ($\delta = \frac{d}{a}$) versus the quality factor Q for the oscillation. Curves are for an $l = 3.0$ meter (solid blue), 2.0 meter (dashed red) and 1.0 meter pendulum (dotted green). (b) For the same pendulum lengths as in (a), the distance versus time relationship for the driving pulse.

High Q pendulums need to be pushed closer to the origin, whereas dissipative pendulums need to be pushed further out. This is shown in Figure 3 in [21], reproduced as Figure 4.2 here. We can relate the quality factor to the free decay period directly by using the classical response of a damped harmonic oscillator $x(t) = ae^{-\frac{t}{\tau}}\sin\omega_0 t$, therefore the momentum loss between $t = 0$ and $t = \frac{T}{2}$ is given by $ma\omega_0\left(1 - e^{-\frac{T}{2\tau}}\right) \cong ma\omega_0\frac{T}{2\tau}$. So, the quality factor can therefore be expressed as,

$$Q = \frac{\pi}{2} \frac{ma\omega_0}{ma\omega_0} \frac{T}{2\tau} = \frac{\pi\tau}{T}.$$

(50)

Substituting equation (50) into (49) leads to the following after restoring the dimensional quantities,

$$\frac{3}{4} \left(\frac{\pi\tau}{T} \right) \left(\frac{a}{l} \right)^2 = \frac{a}{d} \sqrt{1 - \left(\frac{d}{a} \right)^2} \cos^{-1} \frac{d}{a}.$$

We know that $\frac{\pi}{T} = \frac{\omega_0}{2}$ and $\omega_0 = \sqrt{\frac{g}{l}}$ so the equation above becomes,

$$\frac{3}{8} \sqrt{\frac{g}{l}} \left(\frac{a}{l} \right)^2 \tau = \frac{\sqrt{a^2 - d^2}}{d} \cos^{-1} \frac{d}{a}. \quad (51)$$

It is shown in [21] that F_{\perp} and F_{\parallel} are related through the dipole-dipole repulsion effect within the magnetic field relations, and within that relationship that there is a minor dependence on b , through the ratio $\left(\frac{b}{d}\right)^2$. However, this ratio is numerically very small, of $\mathcal{O}(0.01)$, in comparison with the principal terms in the expression, so, as shown in [21], it is entirely justifiable to ignore this dependency. The pusher 'on time' t_d can now be calculated from the following algorithmic procedure:

(a) measure experimentally the period T , (b) select an amplitude a based on suitable launch displacement IC, (c) measure experimentally the free decay period τ , (d) select nominal pendulum length l , (e) compute α , (f) then compute Q from equation (50), (g) use equation (49) to get δ , and hence d , (h) finally, calculate t_d from $t_d = \frac{1}{\omega_0} \sin^{-1} \frac{d}{a}$.

4.2 Electromagnetic excitation of the pendulum

The equations of motion for the Foucault pendulum have been derived by Cartmell *et al* [23] in terms of local Cartesian coordinates, and are then developed there for the case of principal parametric excitation of the length [23, 24]. Here we exclude parametric excitation and instead replace this with a generalised force term in each equation representing the x and y components of the applied electromagnetic dipole force respectively. Reproducing the equations of motion for the unforced pendulum from [23] and including the generalised forces Q_x and Q_y ,

$$\begin{aligned} \ddot{x} + \eta|\dot{x}|\dot{x} - 2\dot{y}\Omega\sin\phi - x\Omega^2 + \frac{gx}{l\sqrt{1 - \frac{x^2 + y^2}{l^2}}} &= Q_x \\ \ddot{y} + \eta|\dot{y}|\dot{y} + 2\dot{x}\Omega\sin\phi - y\Omega^2\sin^2\phi + r\Omega^2\sin\phi\cos\phi + \frac{gy}{l\sqrt{1 - \frac{x^2 + y^2}{l^2}}} &= Q_y. \end{aligned} \quad (52)(53)$$

The excitation system, based closely on the proposals in [21], comprises two concentric coils with an outer sense coil and an inner exciter coil. The electromagnetic dipole force results from the interaction from a permanent neodymium magnet in the base of the bob and the inner exciter coil as the bob passes above. The exciter coil is driven by a high current low voltage supply which is pulsed electronically as the bob is detected by the outer sense coil, and so the form of the

electromagnetic force pulse is broadly square, and in phase with the pendulum swing as the bob passes across the coils, noting that this is where the swing velocity is at a maximum. From this we get the generalised forces, as follows,

$$Q_x = F_x \cos(\tan^{-1} \frac{y}{x}), \quad Q_y = F_y \cos(\tan^{-1} \frac{y}{x}) \quad (54)(55)$$

The excitation components F_x and F_y are pulsatile and can be modelled by use of an inverse tangent function where the argument is the relevant component velocity divided by a scaling parameter k , and suitable pulse shaping, with dipole force magnitude F_{dip} . Clearly F_x and F_y are analogous to F_{\parallel} and F_{\perp} in section 4.1 but we use the notation F_x and F_y here in order to distinguish between the uses of these forces for ellipticity control and for general excitation of the pendulum. After division through by the bob mass M the components can be stated as,

$$F_x = \frac{2 F_{dip}}{\pi M} \tan^{-1} \left(\frac{\dot{x}}{k} \right), \quad F_y = \frac{2 F_{dip}}{\pi M} \tan^{-1} \left(\frac{\dot{y}}{k} \right) \quad (56)(57)$$

Substituting equations (56) and (57) into (54) and (55) respectively leads to the full forms for the generalised forces,

$$Q_x = \frac{2 F_{dip}}{\pi M} \tan^{-1} \left(\frac{\dot{x}}{k} \right) \cos(\tan^{-1} \frac{y}{x}), \quad Q_y = \frac{2 F_{dip}}{\pi M} \tan^{-1} \left(\frac{\dot{y}}{k} \right) \sin(\tan^{-1} \frac{y}{x}) \quad (58)(59)$$

Equations (58) and (59) are substituted into (52) and (53) respectively and then the system can be numerically integrated, using practical design data.

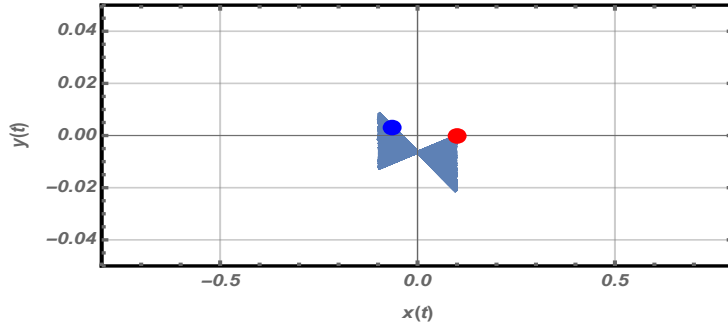


Figure 4.3 Pendulum responses over 1 hour at Glasgow for no excitation ($F_{dip} = 0$). Red dot: displ. ICs $(x_0, y_0) = (0.1, 0) m$, blue dot: end points (x_{tend}, y_{tend}) , velocity ICs are $\dot{x}_0 = \dot{y}_0 = 0 \frac{m}{s}$. Data: $l_0 = 4 m$, $g = 9.8156 m/s^2$, $\Omega_{\oplus} = 7.2921150 * 10^{-5} rad/s$, $\phi = 0.9750 rad$, $r = 6363.18 * 10^3 m$, $m = 2 kg$, $\rho = 1.189 kg/m^3$, $C_D = 10^{-6}$, $R_{bob} = 0.0463134 m$, $t_{end} = 3600 s$. Axes scaled in metres.

Firstly, we show the response of the unforced pendulum just to initial conditions in Figure 4.3, for which $F_{dip} = 0$. The damping is aerodynamic and minimal, so the pendulum shows some precession driven by the rotation of the Earth, Ω_{\oplus} .

In Figure 4.4 the system is under an electromagnetic excitation where $F_{dip} = 0.05 \text{ N}$, $k = 0.01$, and $t_{end} = 360 \text{ s}$, all other data are identical to that of Figure 4.3. Amplification is evident, and is based directly on the form of electromagnetic excitation used, such that this excitation can effectively eradicate the tendency to ellipticity for even relatively short pendulums [21].

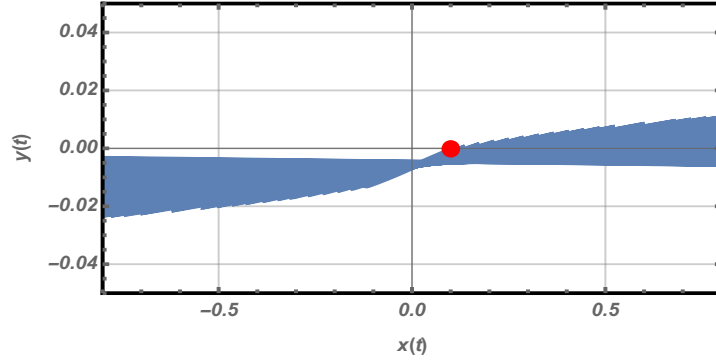


Figure 4.4 Pendulum responses over 6 minutes at Glasgow for excitation $F_{dip} = 0.05 \text{ N}$. Red dot: displ. ICs $(x_0, y_0) = (0.1, 0) \text{ m}$, blue dot: end points (x_{tend}, y_{tend}) , velocity ICs are $\dot{x}_0 = \dot{y}_0 = 0 \frac{\text{m}}{\text{s}}$. Data: $l_0 = 4 \text{ m}$, $g = 9.8156 \text{ m/s}^2$, $\Omega_{\oplus} = 7.2921150 * 10^{-5} \text{ rad/s}$, $\phi = 0.9750 \text{ rad}$, $r = 6363.18 * 10^3 \text{ m}$, $m = 2 \text{ kg}$, $\rho = 1.189 \text{ kg/m}^3$, $C_D = 10^{-6}$, $R_{bob} = 0.0463134 \text{ m}$, $t_{end} = 360 \text{ s}$, $k = 0.01$. Axes scaled in metres.

The generalised forces in equations (58) and (59) can be plotted against time and then related in terms of phase to the pendulum responses in x and y , as shown in the plots of Figure 4.5 taking a snap-shot in time of Q_x and also of the response in x . The mid-point of the excitation pulse Q_x coincides with the zero-crossing of the pendulum in x where it reaches its maximum velocity. The very high amplitude gain in x for the particular level of generalised force applied, is quite evident here.

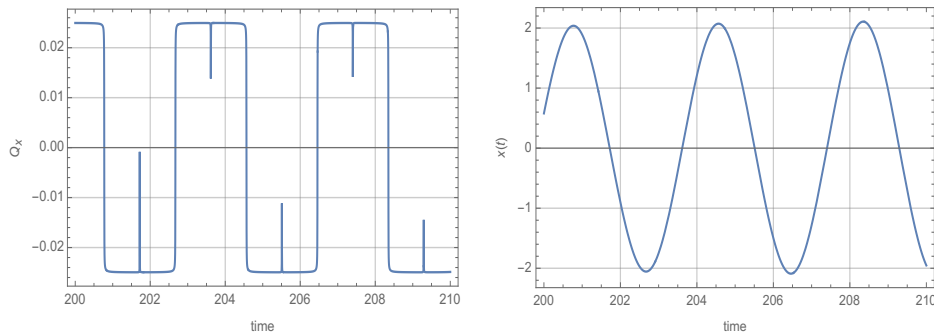


Figure 4.5 Left plot: a snap-shot of the square-wave generalised force $Q_x \text{ (N)}$ against time (s) . Right plot: a snap-shot of the response of the pendulum in $x \text{ (m)}$ against exactly the same window of time (s) , both plots for the data of Figure 4.4.

Conclusions

In this paper a derivation is summarised for a simple expression for the Lense-Thirring precession of a test mass in the vicinity of the Earth, using gravitoelectromagnetism, and under the restrictions of locally flat Euclidean space, weak fields, and non-relativistic velocities. The North Pole is used as a basis for predictive comparison and the approximate expression for Lense-Thirring precession derived in this paper shows a very good level of agreement with previously published predictions for that location ($\sim 0.2\%$). The prediction also accounts for numerically symmetrical latitudes either side of the equator and for Earth oblateness. From there the paper discusses how a practical terrestrial measurement of Lense-Thirring precession may be made, referring to the seminal proposals of [15] for a possible polar measurement. An analysis of the correction term needed for non-polar measurement location is given and it is shown that minute variations in the local acceleration due to gravity, g , over time at non-polar locations generate correspondingly large fluctuations in the correction terms. These fluctuations are of a magnitude which would swamp the required Lense-Thirring precession, and so it is concluded that appropriate signal processing analysis needs to be introduced in order to recognise this part of the composite data and extract it accordingly. This is reserved for further work planned for the near future. The paper then goes on to propose a methodology for optical tracking geometry from which relativistic deviations from the Newtonian precession of the pendulum bob can be detected and logged against time. Three sub-geometries are proposed here, with the first and third of these merely the two extreme cases of the second variant, resulting in a single algorithmic procedure which can be suitably embedded in the data-logging software. From here an ingenious analysis proposed in [21] is examined in some detail, in order to highlight how the work of [21] on an electromagnetic pendulum pusher might be applied to the pendulum system under discussion. The objective is to show that this electromagnetic system could then be analysed in the context of the generalised forces operating on the pendulum, and a discussion of this is given here, showing that the periodic square-wave pulsatile force profile needed to implement the pusher concept of [21] can be arranged in practice. The phase relationship between the generalised force and the response can be seen directly in the results given, confirming that the centres of the square wave excitation pulses, in both the positive and negative excursions, coincide exactly with the zero crossings of the response of the pendulum where it is moving with maximum velocity. This confirms the utility of the design given in [21] in the current context, and provides a framework for practical implementation and test.

In overall terms this paper provides a series of coherent analyses that are required as a basis for building an instrument using a Foucault pendulum for the terrestrial, non-polar, measurement of the frame-dragging effect of Lense-Thirring precession. Whilst the achievement of this goal is still a work in progress the proposals summarised in this paper provides a considerable step forward.

Acknowledgements

The author would like to thank the following people for their valuable comments and suggestions: J.E.Faller, N.A.Lockerbie, R.Schumacher, and K.S.Thorne. Acknowledgement is also due to the University of Strathclyde for on-going access to laboratory facilities.

References

1. G. Chartas, Frame Dragging, Department of Physics & Astronomy, College of Charleston, SC 29424, USA, (last accessed 2 November 2021) <http://chartasg.people.cofc.edu/chartas/Teaching.html>
2. Lense-Thirring precession, Wikipedia, (last accessed 2 November 2021) https://en.wikipedia.org/wiki/Lense%E2%80%93Thirring_precession
3. Gravity Probe B, Wikipedia, (last accessed 2 November 2021) https://en.wikipedia.org/wiki/Gravity_Probe_B
4. B. Tapley, I. Ciufolini, Measuring the Lense-Thirring precession using a second Lageos satellite, Report No. CSR-89-3, Center for Space research, The University of Texas at Austin, TX 78712, USA, September 30 1989.
5. The Geodetic effect, Wikipedia, (last accessed 2 November 2021) https://en.wikipedia.org/wiki/Geodetic_effect
6. J. Kolena, General Relativistic Frame Dragging, North Carolina School of Science and Mathematics, Duke University, NC 27705, USA. <http://webhome.phy.duke.edu/~kolena/ncssm.html> (last accessed 2 November 2021).
7. D. Butler, General Relativity II – Effects, (last accessed 2 November 2021) <http://howfarawayisit.com/>
8. O. Chashchina, L. Iorio, Z. Silagadze, Elementary derivation of the Lense-Thirring precession, *Acta Physica Polonica B*, **40** (8), pp 2363-2378, 2009.
9. M.P. Hobson, G. Efstathiou, and A.N. Lasenby, General Relativity: an introduction for physicists, Cambridge University Press, 2006.
10. J.F. Pascuel-Sánchez, TELEPENSOUTH project: Measurement of the Earth gravitomagnetic field in a terrestrial laboratory, arXiv:gr-qc/0207122v1, 30 July 2002.
11. L.I. Schiff, Possible new experimental test of general relativity theory, *Physical Review Letters*, **4**(5), pp 215-217, 1960.
12. M.L. Ruggiero, A. Tartaglia, Gravitometric Effects, arXiv:gr-qc/0207065v2, 8 February 2008.
13. J.B. Hartle, Gravity: An Introduction to Einstein's General Relativity, Addison-Wesley, 2003.
14. A.B. Pippard, The parametrically maintained Foucault pendulum and its perturbations, *Proc. Royal Soc. London A*, **420**, pp 81-91, 1988.
15. V.B. Braginsky, A.G. Polnarev, and K.S. Thorne, Foucault pendulum at the South Pole: Proposal for an experiment to detect the Earth's general relativistic gravitomagnetic field, *Physical Review Letters*, **53**, 9, pp 863-866, August 1984.
16. WSG-84 terrestrial gravity model (last accessed 2 November 2021) https://en.wikipedia.org/wiki/Gravity_of_Earth
17. WSG-84 local gravity online calculator, (last accessed 2 November 2021), http://the-mostly.ru/misc/local_gravity_online_calculator.html
18. World elevation map finder, (last accessed 2 November 2021), https://elevation.maplogs.com/poi/glasgow_city_uk.97258.html
19. R.P. Middlemiss, S.G. Bramsiepe, R. Douglas, S. Hild, J. Hough, D.J. Paul, A. Samarelli, S. Rowan, G.D. Hammond, Microelectromechanical system gravimeters as a new tool for gravity imaging. *Philosophical Transactions*

- of the Royal Society A*, 376, 20170291.
<http://dx.doi.org/10.1098/rsta.2017.0291>, 2017.
20. International Earth Rotation and Reference Systems Service, (last accessed 2 November 2021), https://www.iers.org/ IERS/EN/Home/home_node.html
 21. R. Schumacher, and B. Tarbet, A short Foucault pendulum free of ellipsoidal precession. [arXiv:0902.1829 \[physics.class-ph\]](https://arxiv.org/abs/0902.1829) (2009)
15 November 2020.
 22. M.G. Olsson, The precessing spherical pendulum, *American Journal of Physics*, 46, 1118, doi: 10.1119/1.11151, 1978.
 23. M.P. Cartmell, J.E. Faller, N.A. Lockerbie, and E. Handous, On the modelling and testing of a laboratory-scale Foucault pendulum as a precursor for the design of a high-performance measurement instrument, *Proceedings of the Royal Society A*, 476, 20190680.
<http://dx.doi.org/10.1098/rspa.2019.0680>, 2019.
 24. M.P. Cartmell, N.A. Lockerbie, and J.E. Faller, Towards a high-performance Foucault pendulum, *Proceedings of the 2nd International Nonlinear Dynamics Conference*, Sapienza University, Rome, Italy, February 16-19, 2021.